Acta Geochim (2019) 38(2):277–291
https://doi.org/10.1007/s11631-018-0292-5

ORIGINAL ARTICLE

Chemical and boron isotopic compositions of tourmaline in the Longtoushan hydrothermal gold deposit, Guangxi, China: implications for gold mineralization

Lihua Qian[1] · Jianqing Lai[1] · Shugen Zhang[1] · Lifang Hu[1] · Rong Cao[1] · Shilong Tao[1]

Received: 19 March 2018 / Revised: 3 July 2018 / Accepted: 7 August 2018 / Published online: 5 September 2018

Abstract The Longtoushan hydrothermal gold deposit is located in the southwestern region of the Dayaoshan Uplift. Tourmaline is widespread in the Longtoushan gold deposit and is mainly distributed in the rhyolite porphyry and associated cryptoexplosive breccia. The spatial distribution of tourmaline enrichment is similar to that of the gold orebody. Feldspar has been largely replaced by tourmaline in the rhyolite porphyry and cryptoexplosive breccia. Electron microprobe analysis revealed that tourmalines in the Longtoushan deposit belong mainly to the alkali group and partly to the X-vacant group; they mostly fell in the schorl-dravite series field. Two distinct sets of dominant substitutions were observed: $MgFe_{-1}$ and $Al\square(NaR^{2+})_{-1}$, where R = Fe, Mg. In addition, minor substitutions include $(CaMg)(NaAl)_{-1}$ and $FeAl_{-1}$. The calculated $\delta^{11}B$ value for the mineralizing fluids ranged from − 12.8 to − 9.7‰, which is typical of S-type granites, and boron-enriched fluids predominantly derived from rhyolitic melt. Part of the tourmaline from the rhyolite porphyry crystallized during the magmatic-hydrothermal stage, whereas most tourmalines from the deposit formed in the post-magmatic hydrothermal stage. The tourmalines were deposited from a relatively reduced and acidic fluid system, and the gold predominantly precipitated during the post-magmatic hydrothermal stage in the Longtoushan deposit.

✉ Jianqing Lai
ljq@csu.edu.cn

[1] Key Laboratory of Metallogenic Prediction of Nonferrous Metals and Geological Environment Monitoring, Ministry of Education, School of Geosciences and Info-Physics, Central South University, Changsha 410083, China

Keywords Longtoushan gold deposit · Tourmaline · Ore-forming fluids · Boron isotopes

1 Introduction

Tourmaline forms in a variety of settings, including as a significant mineral crystallizing in fractionated igneous bodies; as a diagenetic mineral in buried sedimentary basins; and as a gangue mineral in ore deposits, associated with contact, regional, and subduction-related metamorphism in metasomatism (e.g., Henry and Dutrow 1996; Slack 1996; Marschall et al. 2009; Hinsberg et al. 2011). Tourmaline is stable under an extensive range of pressures and temperatures that cover most of the geological settings found in Earth's crust, and it can exist in equilibrium with a variety of geological fluids (e.g., Huang et al. 2008; Novák et al. 2011; Dutrow and Henry 2011; Hinsberg et al. 2011). The major and trace element chemistry of hydrothermal tourmaline is controlled by the host rock, the external hydrothermal fluids, and the pressure–temperature conditions of tourmaline crystallization (e.g., Henry and Guidotti 1985; Codeço et al. 2017). In fluid-dominated systems, such as breccia pipes and veins, tourmaline chemistry is generally buffered by the fluid phase (Slack and Coad 1989; Slack and Trumbull 2011). Mineralogical, chemical and boron isotopic analyses of tourmaline have been used to better constrain ore-forming processes (Slack and Trumbull 2011; Xiong et al. 2014).

The Longtoushan hydrothermal gold deposit, which is associated with cryptoexplosive breccias, is located in the southwestern region of the Dayaoshan Uplift (Fig. 1). Gold mineralization can be divided into two types in the deposit: (1) disseminations or veins in the rhyolite porphyry and cryptoexplosive breccia, and (2) veins or stockworks in the

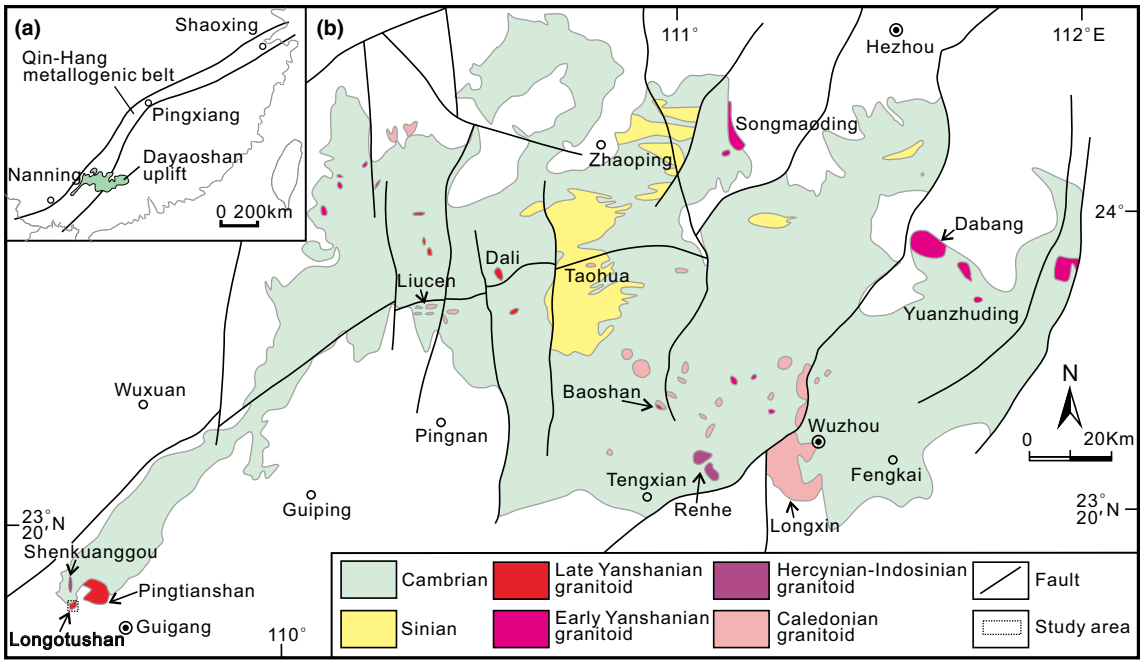

Fig. 1 **a** Sketch map showing the location of the Dayaoshan Uplift in the Qinzhou–Hangzhou metallogenic belt, South China. **b** Sketch map of the Dayaoshan Uplift. Modified after Chen et al. (2015)

clastic rocks of the Lianhuashan Formation (Xie and Sun 1993; Yang et al. 2008; Wang 2011). Tourmaline, mainly distributed in the rhyolite porphyry and cryptoexplosive breccia, is closely related to gold mineralization, and crystallized in the early stage of the pneumatic-hypothermal episode (Xie and Sun 1993; Huang et al. 1999). Nevertheless, few studies have been performed on the tourmaline from this deposit. Lu (2008) briefly described the occurrence and composition of tourmaline in the gold orebody of the Longtoushan deposit, suggesting that it belongs to the schorl-dravite series. Based on petrographic and electron microprobe analysis of tourmalines from the Longtoushan deposit, Wang (2011) emphasized that tourmalines above the 420-m level are rich in Fe and depleted in Mg, and those below 420 m are rich in Mg. However, previous studies of tourmaline from the Longtoushan deposit did not concentrate on its genesis and relationship to mineralization. This paper presents mineralogical-textural characteristics and chemical and boron isotopic compositions of tourmaline from the Longtoushan gold deposit. These results, combined with relevant data from Wang (2011), were used to constrain the early evolution of ore-forming fluid in the Longtoushan gold deposit.

2 Geological setting

2.1 Regional geology

The Qinzhou–Hangzhou metallogenic belt, located in the Neoproterozoic collisional orogen between the Yangtze and Cathaysia Blocks, is a major polymetallic (Cu, Mo, W, Sn, Pb, Zn, Au, and Ag) belt in South China (Mao et al. 2011; Zhou et al. 2012). The Dayaoshan Uplift consists of weakly metamorphosed basement, and is situated in the southwestern margin of the Qinzhou–Hangzhou metallogenic belt (Fig. 1a). The strata exposed in this area consist mainly of the Sinian Peidi Formation and the Cambrian Xiaoneichong and Huangdongkou Formations, composed dominantly of greywackes with some interlayers of argillites and silty shales (Bureau of Geology and Mineral Resources of Guangxi Zhuang Autonomous Region 1985). The main structures in the region include the EW-trending Dayaoshan anticlinorium and the Dali deep fault, on which NE-, NW-, and SN-trending structures superimposed (Fig. 1b). Widespread magmatic intrusions in the Dayaoshan area include granite, biotite granite, monzogranite, and granodiorite, formed during four stages: Caledonian (470–430 Ma), Hercynian–Indosinian (270–240 Ma), early Yanshanian (170–150 Ma), and late Yanshanian (110–90 Ma) (Chen et al. 2015). The Caledonian and Yanshanian granitoids are the most abundant felsic igneous rocks in the Dayaoshan area, and are accompanied by

abundant igneous related W–Mo–Cu–Au–Ag–Pb–Zn polymetallic mineralization (Huang et al. 2003).

2.2 Local geology

The main lithostratigraphic units that outcrop in the Longtoushan gold deposit include the Cambrian Huangdongkou Formation and the Lower Devonian Lianhuashan Formation (Fig. 2a). The former is composed of low-grade metamorphic fine-grained sandstone, argillaceous siltstone, carbonaceous slate, and spotted slate; the latter consists of conglomerate, sandy conglomerate, quartz sandstone, fine-grained sandstone, and argillaceous siltstone. The faults in this deposit are NW-, NS-, NE-, or EW-striking. The NW-striking faults, which are characterized by long extensions, deep depths, and steep dips, are the main ore-controlling structures in the deposit (Xie and Sun 1993). The Longtoushan granitic complex has an irregular, oval shape horizontally and a pipe shape vertically (Fig. 2b), dipping steeply to the northwest. It is mainly composed of biotite granite porphyry and subvolcanic sequences, including cryptoexplosive breccia, rhyolite porphyry, monzogranite porphyry, and felsic dykes. Zircon SHRIMP U–Pb ages of monzogranite porphyry and rhyolite porphyry yield 100.3 ± 1.4 Ma and 103.3 ± 2.4 Ma, respectively (Chen et al. 2008), suggesting that the gold mineralization at the Longtoushan deposit occurred in the late Yanshanian. Additionally, the granites are considered to be S-type granitoids (Duan et al. 2011; Wang 2011).

The gold orebodies are dominantly hosted within the contact zone of the rhyolite porphyry and cryptoexplosive breccia (Fig. 2b), and partly distributed in the fault or fracture zone of the wall rock. Additionally, porphyry-style Cu mineralization has been discovered in the granite porphyry at depth (∼ 70 m above sea level) (Huang et al. 1999). Gold orebodies, which are vein-like, lenticular, and cystic with dip angles of 76° to 90°, are mostly NW-trending in the deposit. Inflation, contraction, branching, compounding, pinching, and recurring occur along the strike and dip of the orebodies. The main metallic minerals are native gold, pyrite, chalcopyrite, chalcocite, arsenopyrite, and bismuthinite, while the major nonmetallic minerals are quartz, tourmaline, sericite, and kaolinite. Wall-rock alteration is pervasive in the Longtoushan gold deposit. Tourmalinization and silicification are predominantly distributed in the rhyolite porphyry and cryptoexplosive breccia and their contact zone, while K-feldspar, sericite, and argillic alteration are mainly hosted in the granite porphyry.

A number of fluid inclusion studies have been performed on the Longtoushan deposit. According to Xie and Sun (1993), Huang et al. (1999), and Zhu (2002), the ore-

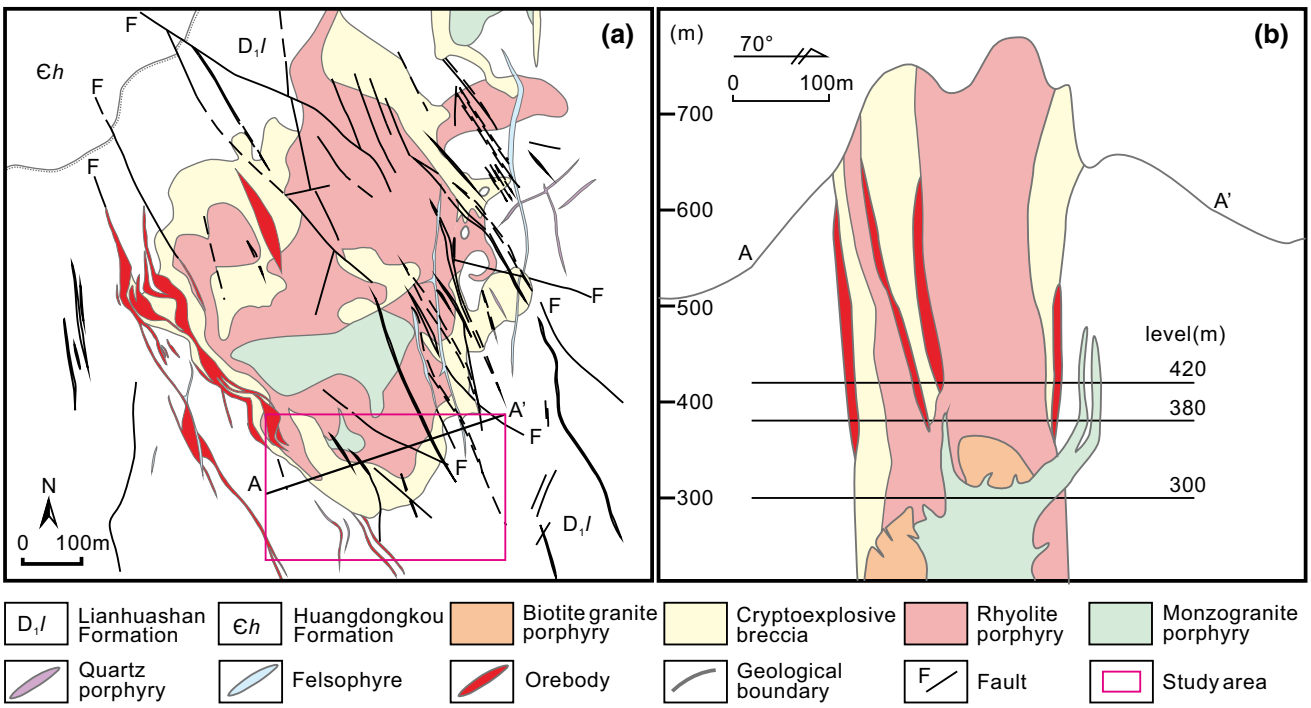

Fig. 2 **a** Geologic map and **b** cross-section profile of the Longtoushan gold deposit. **a** is modified after Xie and Sun (1993)

forming temperature of the Longtoushan gold deposit may range from 160 to 320 °C, 170 to 560 °C, or 180 to 290 °C, respectively. Salinities of the fluid inclusions vary between 9.4 and 53.6% NaCl eq (Huang et al. 1999). Group fluid inclusions analyses suggest that the fluids are dominated by Na^+, K^+, Ca^{2+}, and Mg^{2+} cations; Cl^-, F^-, and SO_4^{2-} anions; and H_2O, CO_2, CO, and CH_4 molecules (Xie and Sun 1993; Huang et al. 1999; Zhu 2002). The $\delta^{34}S$ values of pyrites range from + 0.6 to + 2.5‰, indicating deeply sourced magmatic sulfur (Xie and Sun 1993; Zhu 2002; Tao et al. 2017). The ore-forming materials are directly derived from the remelting of granitic magma; the fluids originate mainly from a magmatic source with an involvement of meteoric water as indicated by hydrogen and oxygen isotopes (Xie and Sun 1993; Huang et al. 1999; Zhu 2002).

3 Tourmaline occurrences

Tourmaline, generally fine-grained, occurs as spot-like, veined and disseminated structures or fillings in geodes with quartz in the Longtoushan gold deposit. According to Xie and Sun (1993), native gold is generally distributed in quartz-tourmaline veinlets. Tourmaline in the deposit was classified by its occurrence: (1) dense dissemination in the rhyolite porphyry (Fig. 3a, b); (2) dissemination in the cement of cryptoexplosive breccia (Fig. 3c); (3) inhomogeneous dissemination in the monzogranite porphyry (Fig. 3d); (4) veinlet-dissemination in the biotite granite porphyry (Fig. 3e); and (5) dissemination in quartz–pyrite veins in sandstone of the Lianhuashan Formation (Fig. 3f).

Feldspar in the rhyolite porphyry was observed to be completely replaced by euhedral to subhedral tourmaline (Fig. 4a), making up 25–40 vol.% of the rhyolite porphyry. A minor amount of corroded quartz phenocrysts displayed growth rim containing fine-grained tourmaline (Fig. 4b). The content of tourmaline in cryptoexplosive breccia, chiefly distributed in the cement, was also high. Biotite and feldspar in the breccias were commonly replaced by tabular and radial aggregates of tourmaline. Biotite and feldspar phenocrysts in the monzogranite porphyry were locally replaced by tourmaline, quartz, sericite, and pyrite; tourmalinization was weak in the matrix and associated with sericitization. Moreover, tourmaline partly exhibited oscillatory zoning in optical and backscattered electron (BSE) images (Fig. 4c). Tourmalinization in the sandstones of the Lianhuashan Formation intensified toward the Longtoushan subvolcanic rocks, reaching contents of up to 25%. Tourmaline generally displayed acicular-prismatic habit in quartz–pyrite veins in the sandstone (Fig. 4d). In addition, rutile associated with tourmaline (Fig. 4e) was

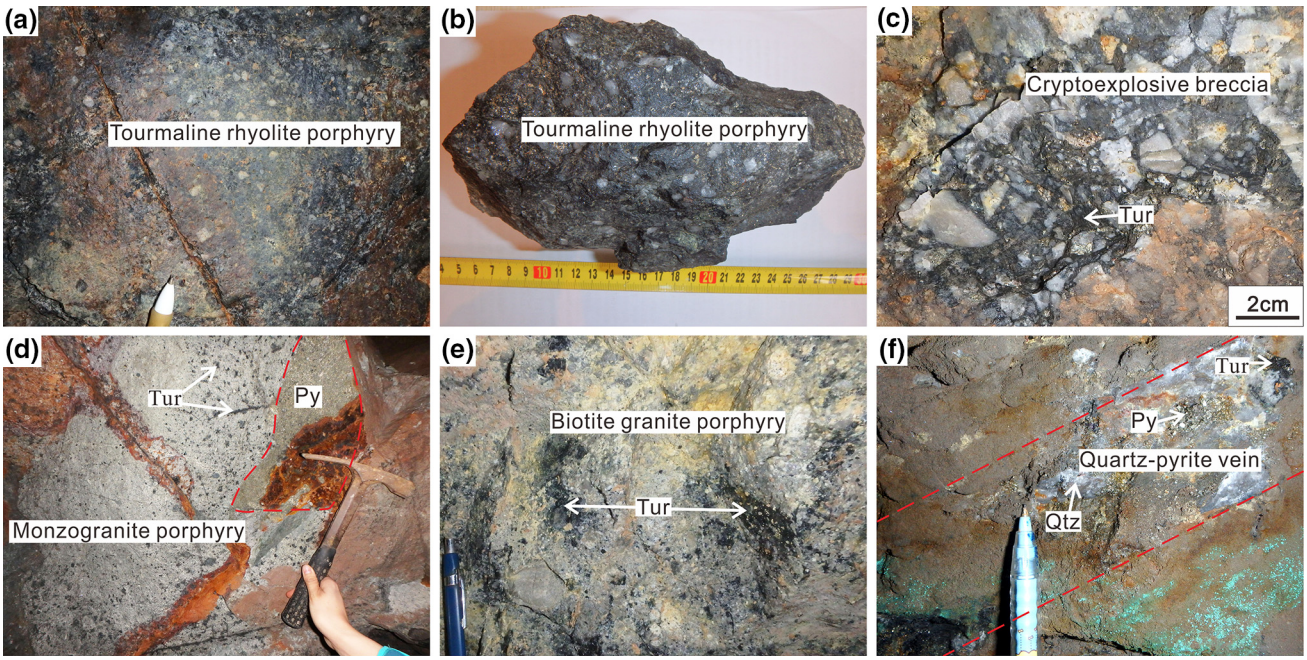

Fig. 3 Photographs showing tourmaline occurrences in the Longtoushan deposit. **a**, **b** Tourmaline disseminated in the rhyolite porphyry; **c** Tourmaline mainly distributed in the cement of cryptoexplosive breccias; **d** Tourmaline in the monzogranite porphyry (inhomogeneous dissemination); **e** Biotite granite porphyry with tourmalinization; and **f** Tourmaline in the quartz–pyrite veins from sandstone. *Tur* tourmaline, *Py* pyrite, *Qtz* quartz

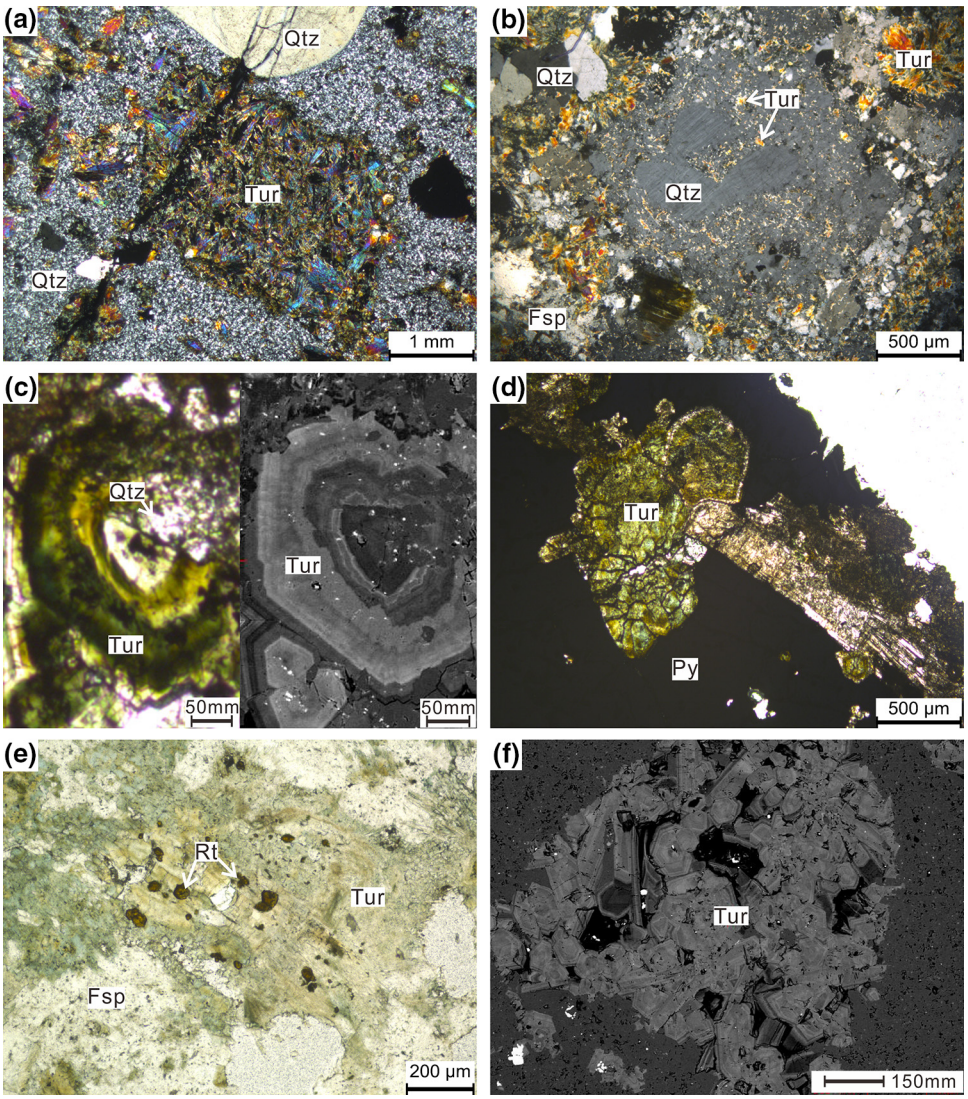

Fig. 4 Photomicrographs of tourmaline from the Longtoushan deposit. **a** Tabular aggregate of tourmaline (Tur) from rhyolite porphyry is pseudomorphic after feldspar phenocryst, transmitted light (+). **b** The growth rim of quartz phenocryst in rhyolite porphyry contains fine tourmaline, transmitted light (+). **c** Photomicrograph [left hand side, transmitted light (−)] and backscattered electron (BSE) image showing optical and compositional zoning in tourmaline. **d** Euhedral tourmaline from sandstone, transmitted light (−). **e** Rutile is chiefly disseminated in tourmaline, transmitted light (−). **f** BSE image showing compositional zoning in tourmaline. "−" means under plane-polarized light; "+" means under cross-polarized light. *Tur* tourmaline, *Qtz* quartz, *Fsp* feldspar, *Py* pyrite, *Rt* rutile

mainly distributed in the monzogranite porphyry and quartz–pyrite–tourmaline veins.

Tourmaline was observed to be dominantly distributed on the edge of the biotite granite porphyry and occurred in veinlet-disseminated morphologies. Biotite and feldspar phenocrysts were observed to be partly replaced by tourmaline, sericite, and pyrite, or completely replaced by tourmaline, quartz, and muscovite. Additionally, the tourmaline generally exhibited oscillatory zoning (Fig. 4f) in the biotite granite porphyry.

4 Sampling and methods

We performed a geological survey on levels between 300 and 420 m a.s.l. (above sea level) in the southern part of the Longtoushan deposit (Fig. 2). In total, 165 samples were collected from those sections. Among them, 127 samples were collected from the 380-m level at 10 m intervals. The petrography of these samples was studied with a conventional polarizing microscope. Duplicate samples from the 380-m level were crushed to a size of 200 mesh and were submitted to the Guilin Research Institute

Table 1 Locations and host rocks of samples

Sample	Location	Host rock
SL-25	Middle section 300 m	Quartz–pyrite–tourmaline vein in sandstone of the Lianhuashan formation
SL-58	Middle section 340 m	Biotite granite porphyry
SJ-104	Middle section 380 m	Rhyolite porphyry
SL-12	Middle section 300 m	Cryptoexplosive breccia
SL-80	Middle section 360 m	Monzogranite porphyry

of Geology for Mineral Resources for boron analysis by emission spectroscopy with a 2-m grating spectrograph (Oberkochen, GER).

Based on the petrographic analysis of tourmaline, we selected five representative samples with different occurrences. Positions and descriptions of these samples are shown in Table 1. Chemical analyses of tourmaline were performed on polished thin sections using a Shimadzu EPMA-1720 electron microprobe at the Key Laboratory of Metallogenic Prediction of Nonferrous Metals and Geological Environment Monitoring (Central South University), Ministry of Education of China. The microprobe was operated using an accelerating voltage of 15 kv, a beam current of 10 nA, a beam size of approximately 1 μm, and a detection limit of 0.01%. The following reference materials were used: SiO_2 (Si), TiO_2 (Ti), $Y_3Al_5O_{12}$ (Al), $NaAlSi_3O_8$ (Na), Fe_3O_4 (Fe), $MnSiO_3$ (Mn), MgO (Mg), CaF_2 (Ca), and $KAlSi_3O_8$ (K). Tourmaline structural formulae were calculated based on 15 cations in the tetrahedral and octahedral sites (T + Z + Y) (Henry and Dutrow 1996).

We selected four samples from those that were analyzed by microprobe for the determination of the boron isotopic compositions of tourmaline. Boron isotopic compositions were measured in situ on polished thin sections using laser ablation–multicollector–inductively coupled plasma–mass spectrometry (LA-MC-ICP-MS) at the State Key Laboratory of Geological Processes and Mineral Resources, China University of Geosciences, Wuhan. A *Resonetics-S155* laser-ablation system (Boston, USA) and Nu Instruments *Nu Plasma II* ICP-MS (Wrexham, Wales, UK) were combined for these experiments. A 193-nm ArF excimer laser, homogenized by a set of beam delivery systems, was focused on the tourmaline surface. The ablation protocol employed a spot diameter of 33 μm and a repetition rate of 8 Hz for 40 s (equal to 320 pulses). The aerosol produced during ablation was transported using a carrier gas of helium mixed with argon and a small amount of nitrogen, and the mixture was carried into the plasma of the MC-ICP-MS. The $^{11}B/^{10}B$ ratios of standard and test samples were obtained using the above method, and the $\delta^{11}B$ values were calculated using external calibration (SSB method). The tourmaline standard IAEA B-4 ($\delta^{11}B = -8.7‰$) from Tonarini et al. (2003) was used as an external standard. The tourmaline standards IMR RB1 (Hou) and Dai of the Laboratory were used for monitoring. The $\delta^{11}B$ values of tourmaline IMR RB1 obtained during this analysis ranged between − 13.2 and − 13.1‰, consistent with the previous result (− 12.96 ± 0.49‰, 1σ) (Hou et al. 2010).

5 Results

5.1 Distribution of tourmaline

Cryptoexplosive breccia was observed to be dominantly distributed in the contact zone of the rhyolite porphyry, with cement mainly composed of rhyolite porphyry or aggregates of pyrite, tourmaline, fine-grained quartz, and rock debris. Clasts of quartz sandstone, siltstone, and granite porphyry ranged from 0.3 to 4 cm in diameter. The cryptoexplosive breccia gradually transitions into rhyolite porphyry, and the interface between them is irregular. Therefore, we could not completely distinguish cryptoexplosive breccia from rhyolite porphyry at the 380-m level in the southern part of the deposit.

Boron anomalies indicate the distribution of tourmaline in the Longtoushan deposit. Gridding using Kriging method in Surfer 8 (Golden Software, Golden, Colorado, USA) was applied to the boron contents of samples from the 380-m level to produce a boron contour map (Fig. 5). The boron contour map suggests that tourmaline is abundant in the contact zone between the rhyolite porphyry and cryptoexplosive breccias along NW–SE striking faults. The pattern of tourmaline enrichment is similar to the extent of the gold orebody in the Longtoushan deposit.

5.2 Chemical compositions of tourmaline

Crystal-chemical formulae of tourmaline were calculated on the basis of the general structural formula $XY_3Z_6T_6O_{18}(BO_3)_3V_3W$, where X = Na, K, Ca, □; Y = Li, Mg, Fe^{2+}, Mn, Al, Cr, V, Ti, Fe^{3+}; Z = Al, Fe^{3+}, Mg, V, Cr; T = Si, Al, B; V + W = OH^- + F^- + Cl^- = 4 atoms per formula unit (apfu) (Henry et al. 2011; Novák et al. 2011).

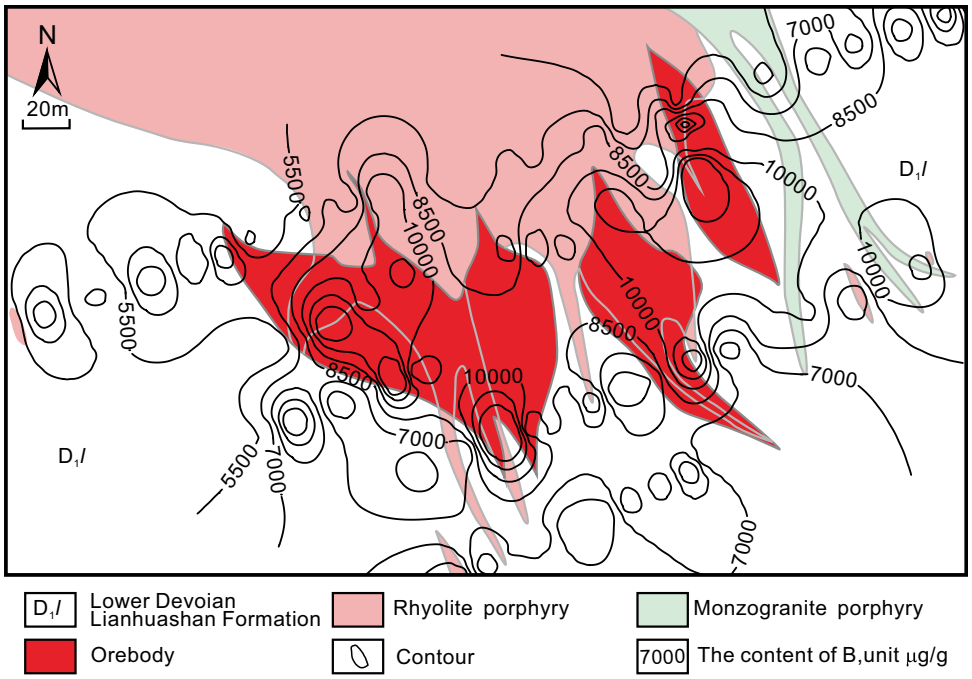

Fig. 5 Boron contour map of the 380-m level in the southern part of the Longtoushan deposit

Representative chemical compositions of tourmalines from the Longtoushan deposit are shown in Table 2. In general, tourmalines were found to belong mostly to the alkali group (Fig. 6a). Tourmalines from the rhyolite porphyry exhibited highly variable X-site vacancies, whereas tourmalines from the cryptoexplosive breccia, biotite granite porphyry, and monzogranite porphyry fell within the alkali group. A minor proportion of tourmalines from veins in sandstone fell in the vacancy group. On the Al–Fe–Mg discrimination diagram (Henry and Guidotti 1985), sampled tourmaline plotted mainly within the fields of Li-poor granitoids and metasedimentary rocks, and predominantly above the schorl-dravite line (Fig. 6b). In addition, tourmaline compositions from the rhyolite porphyry show two distinct clusters (Fig. 6b), and tourmaline from veins in sandstone plotted partly within the field of Fe^{3+}-rich quartz-tourmaline rocks, calc-silicate rocks and metapelites.

Tourmaline from the Longtoushan deposit displayed considerable variations in $Fe_{tot}/(Fe_{tot} + Mg)$ (Table 2). Except for a number of analyses from the rhyolite porphyry and individual sample points from veins in sandstone, which fell within the foitite or "Oxy-foitite" and Mg-foitite fields, tourmaline composition plotted predominantly within the field of the schorl-dravite series (Fig. 7).

5.3 Boron isotopic compositions of tourmaline

Tourmalines from the Longtoushan deposit displayed a narrow range of $\delta^{11}B$ values (Table 3). The $\delta^{11}B$ values of tourmalines from the rhyolite porphyry, cryptoexplosive breccia, biotite granite porphyry and sandstone ranged from − 14.0 to − 12.3‰ (average = − 13.2‰), − 15.4 to − 14.3‰ (average = − 14.7‰), − 14.4 to − 12.3‰ (average = − 13.7‰), and − 15.2 to − 13.3‰ (average = − 14.4‰), respectively.

6 Discussion

6.1 Boron isotope signatures

The $\delta^{11}B$ value of tourmaline is chiefly controlled by the composition of the boron sources (e.g., Palmer and Slack 1989; Jiang et al. 1999). The entrapment stage of fluid inclusions in Xie and Sun (1993) and Zhu (2002) is unclear, thus the relatively low homogenization temperature presented by them may correspond to late stages of mineralization in the Longtoushan deposit. According to Huang et al. (1999), tourmaline formed during two early ore-forming stages with temperatures ranging from 320 to 560 °C. The homogenization temperature peaks of the two stages are 370 and 460 °C, respectively, and the average value of them is approximately 410 °C. Using this as a reasonable estimate for tourmaline formation in the Longtoushan deposit, the hydrothermal fluid would be 2.6‰ heavier in $\delta^{11}B$ than the coexisting tourmaline based on the factors of Meyer et al. (2008). Calculated $\delta^{11}B$ values for the mineralizing fluids ranged from − 12.8 to − 9.7‰, which is typical of S-type granites (Trumbull and

Table 2 Average compositions of tourmaline from the Longtoushan deposit

Host rock	Ryolite porphyry					Cptoexplosive breccia				Monzogranite porphyry			
Level (m)	700	620	460	380		420	380	300		360			
Sample	LTS 700-1[a]	LTS 620-6[a]	LTS 460-17b[a]	SL-104		LTS 420-14[a]	LTS 380-20[a]	SL-12		SL-80			
				Core	Rim			I[b]	II[b]	Core	Rim	I[b]	II[b]
n	9	5	13	6	5	17	6	5	8	3	6	2	4
SiO_2	35.68	35.9	35.62	35.45	35.14	36.76	36.67	34.78	34.20	35.12	33.80	34.38	34.14
TiO_2	0.12	0.11	0.26	0.19	0.28	0.30	0.50	1.17	0.26	0.22	0.53	0.32	0.39
Al_2O_3	35.29	31.26	34.83	37.27	36.52	33.24	33.82	31.57	33.82	35.70	33.08	36.17	35.06
FeO	12.04	13.63	11.89	1.08	4.18	4.95	6.72	7.08	8.54	3.93	7.67	4.46	7.15
MgO	1.08	3	1.35	8.78	6.92	7.18	5.85	7.57	5.93	7.53	7.01	7.71	6.05
MnO	0.01	0.04	0.02	0.02	0.01	0.02	0.02	0.02	0.03	0.02	0.01	0.00	0.00
CaO	0.05	0.2	0.14	0.37	0.27	0.61	0.50	1.28	0.21	0.41	0.56	0.62	0.44
Na_2O	1.31	1.92	1.26	2.19	1.60	2.11	2.10	1.70	2.24	1.92	2.23	2.02	1.91
K_2O	0.01	0.03	0.01	0.02	0.01	0.01	0.01	0.02	0.03	0.03	0.03	0.03	0.04
Total	85.6	86.11	85.37	85.37	84.93	85.18	86.19	85.18	85.26	84.88	84.92	85.71	85.19
Si	6.005	6.066	6.012	5.685	5.715	6.055	6.018	5.791	5.683	5.733	5.629	5.577	5.643
Ti	0.015	0.014	0.033	0.023	0.035	0.037	0.062	0.148	0.033	0.027	0.067	0.039	0.048
Al	7.001	6.223	6.928	7.045	7.001	6.453	6.544	6.189	6.622	6.865	6.491	6.912	6.829
Fe	1.698	1.936	1.684	0.146	0.569	0.691	0.922	0.987	1.188	0.538	1.071	0.606	0.989
Mg	0.270	0.750	0.337	2.099	1.678	1.756	1.430	1.882	1.468	1.834	1.741	1.866	1.490
Mn	0.002	0.006	0.003	0.002	0.001	0.003	0.003	0.003	0.004	0.003	0.002	0.000	0.001
Ca	0.010	0.036	0.025	0.064	0.047	0.107	0.088	0.230	0.038	0.072	0.100	0.101	0.078
Na	0.426	0.631	0.413	0.682	0.504	0.674	0.668	0.548	0.720	0.609	0.720	0.701	0.614
K	0.003	0.007	0.002	0.004	0.002	0.002	0.002	0.004	0.006	0.005	0.005	0.006	0.008
X-Val	0.561	0.326	0.560	0.250	0.447	0.217	0.242	0.218	0.236	0.313	0.175	0.251	0.300
Fe/(Fe+Mg)	0.866	0.719	0.830	0.064	0.255	0.277	0.397	0.346	0.450	0.222	0.377	0.244	0.399

Table 2 continued

Host rock	Biotite granite porphyry		Sandstone						
Level (m)	340		540	347	340	300			
Sample	SL-58		LTS 540-3[a]	ZK1203 -347(2)[a]	LTS 340-6[a]	SL-25			
	Core	Rim				Core	Rim	I[b]	II[b]
n	8	7	8	13	7	6	2	5	6
SiO_2	33.66	34.09	36.29	37.15	36.25	34.71	35.13	34.93	34.02
TiO_2	0.50	0.56	0.57	0.16	0.75	0.69	1.70	0.21	0.75
Al_2O_3	33.64	33.18	32.98	34.32	31.20	32.42	27.89	36.37	30.59
FeO	9.21	7.51	12.24	2.89	4.42	6.92	9.84	2.52	8.03
MgO	5.49	6.58	2.02	7.41	8.85	7.44	7.30	8.57	8.09
MnO	0.02	0.02	0.02	0.01	0.01	0.01	0.01	0.02	0.01
CaO	0.33	0.30	0.24	0.35	1.82	0.51	0.93	0.50	0.72
Na_2O	2.02	2.31	1.61	2.09	1.66	2.31	2.19	1.98	2.45
K_2O	0.02	0.02	0.01	0.03	0.02	0.02	0.03	0.02	0.03
Total	84.88	84.58	85.98	84.41	84.98	85.02	85.02	85.12	84.69
Si	5.637	5.700	6.122	6.104	6.001	5.767	5.960	5.643	5.707
Ti	0.063	0.071	0.072	0.020	0.093	0.087	0.217	0.026	0.095
Al	6.637	6.535	6.555	6.645	6.088	6.341	5.577	6.923	6.048
Fe	1.290	1.054	1.727	0.400	0.615	0.963	1.397	0.341	1.126
Mg	1.372	1.638	0.507	1.813	2.182	1.842	1.847	2.063	2.023
Mn	0.002	0.003	0.002	0.002	0.002	0.001	0.001	0.002	0.001
Ca	0.059	0.054	0.043	0.062	0.321	0.091	0.168	0.087	0.130
Na	0.658	0.751	0.528	0.667	0.536	0.745	0.721	0.621	0.797
K	0.004	0.004	0.003	0.005	0.004	0.004	0.006	0.005	0.005
X-Val	0.279	0.191	0.427	0.266	0.140	0.160	0.105	0.287	0.067
Fe/(Fe+Mg)	0.485	0.386	0.788	0.178	0.216	0.341	0.431	0.141	0.357

[a]Smples LTS700-1, LTS620-6, LTS460-17b, LTS420-14, LTS380-20, LTS540-3, ZK1203-347(2), LTS340-6 are from Wang (2011); [b]SL-12-I-brown tourmaline, SL-12-II-green tourmaline; SL-80-I-sample point located in the outside of the rim, SL-80-II-fine tourmaline grains; SL-25-I-fine acicular tourmaline grains, SL-25-II-fine tourmaline grains

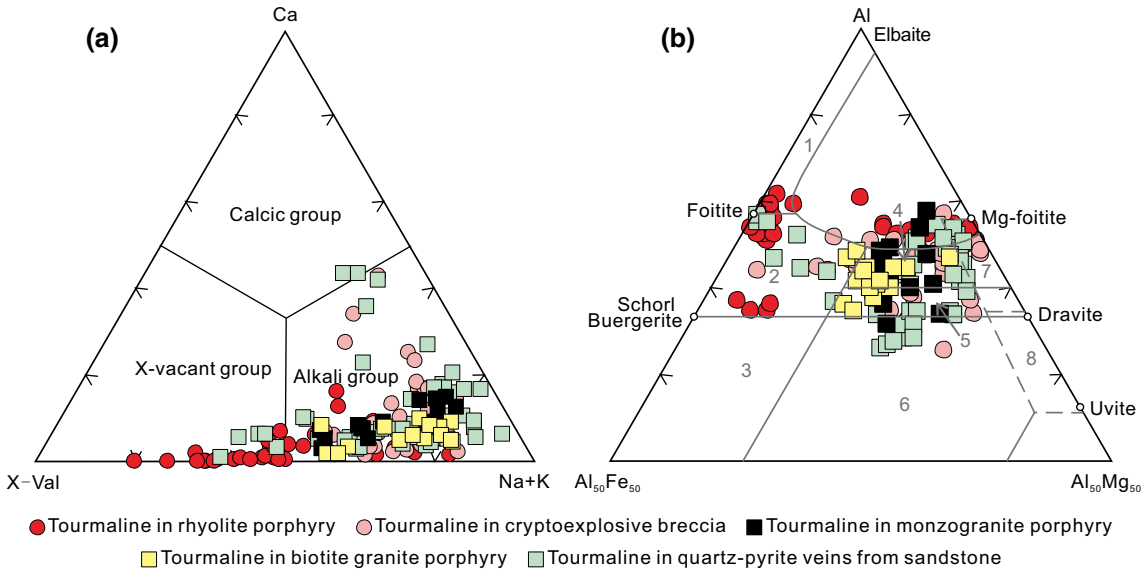

Fig. 6 Composition of tourmaline from the Longtoushan deposit. **a** Ca-X-site vacancy-Na (+K) triangle (Henry et al. 2011). **b** Fe_{tot}–Mg–Al triangle (Henry and Guidotti 1985). In plot **b**: (1) Li-rich granitoid pegmatites and aplites; (2) Li-poor granitoid rocks and associated pegmatites and aplites; (3) Fe^{3+}-rich quartz–tourmaline rocks (hydrothermally altered granites); (4) Metapelites and metapsammites coexisting with an Al-saturating phase; (5) Metapelites and metapsammites not coexisting with an Al-saturating phase; (6) Fe^{3+}-rich quartz–tourmaline rocks, calc-silicate rocks, and metapelites; (7) Low-Ca metaultramafic rocks and Cr, V-rich metasediments; (8) Metacarbonates and meta-pyroxenites

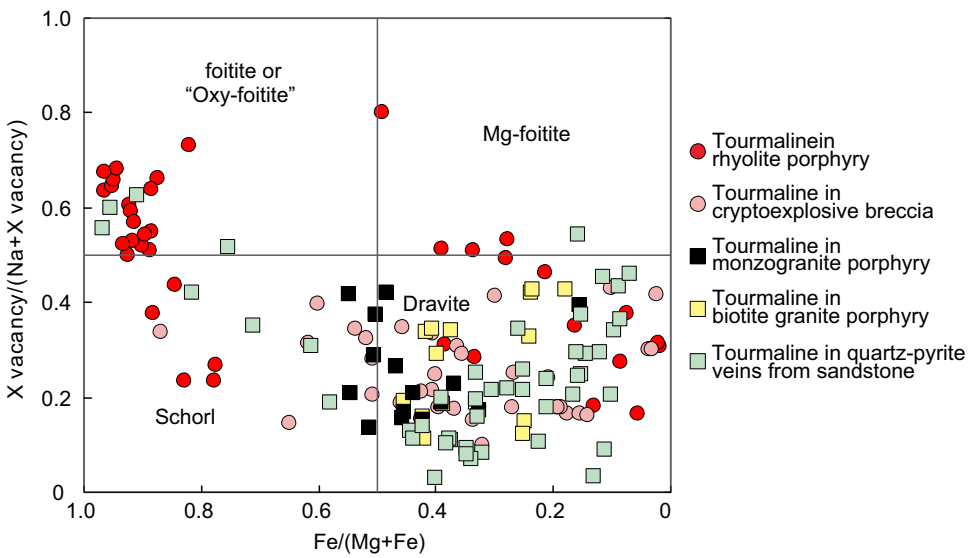

Fig. 7 Compositional discrimination between tourmalines from the Longtoushan deposit in terms of Fe/(Fe + Mg) versus X vacancy/(Na + X vacancy), atoms or atom equivalents

Slack 2018). A 240 °C gradient in the temperature of tourmaline growth corresponds to a difference of 3.8‰ in the fractionation effect, which largely corresponds to the observed variation in the boron isotope compositions of tourmaline. In addition, ^{11}B partitions preferentially into H_2O fluid and ^{10}B into illite, muscovite, and silicate melt (Hervig et al. 2002), which may have led to the slightly heavier $\delta^{11}B$ values of tourmalines from the rhyolite porphyry and biotite granite porphyry than those from the cryptoexplosive breccias and sandstone.

The modal percentage of tourmaline (up to about 40 vol.%) in the rhyolite porphyry and cryptoexplosive breccia implies that the high boron concentration must have derived externally and that the isotopic composition of boron in tourmaline is dominated by that of the hydrothermal fluid. Furthermore, the tourmaline enrichment zone is concentrated in the contact between the rhyolite porphyry and cryptoexplosive breccia, and the rhyolite porphyry evolved from S-type melt (Duan et al. 2011). Consequently, boron-rich ore-forming fluids that led

Table 3 Boron isotopic compositions of tourmaline from the Longtoushan deposit

Analysis no.	Host rock	$\delta^{11}B$ (‰)	1σ (‰)
SL104-1	Rhyolite porphyry	− 13.2	0.165
SL104-2	Rhyolite porphyry	− 12.3	0.156
SL104-3	Rhyolite porphyry	− 13.8	0.164
SL104-4	Rhyolite porphyry	− 13.5	0.207
SL104-5	Rhyolite porphyry	− 14.0	0.172
SL104-6	Rhyolite porphyry	− 12.9	0.292
SL104-7	Rhyolite porphyry	− 13.4	0.334
SL104-8	Rhyolite porphyry	− 12.4	0.329
SL12-1	Cryptoexplosive breccia	− 14.4	0.237
SL12-2	Cryptoexplosive breccia	− 14.5	0.179
SL12-4	Cryptoexplosive breccia	− 15.4	0.156
SL12-5	Cryptoexplosive breccia	− 14.3	0.147
SL12-6	Cryptoexplosive breccia	− 15.2	0.165
SL12-7	Cryptoexplosive breccia	− 14.8	0.161
SL12-8	Cryptoexplosive breccia	− 14.7	0.165
SL12-9	Cryptoexplosive breccia	− 14.5	0.164
SL58-1	Biotite granite porphyry	− 13.9	0.247
SL58-2	Biotite granite porphyry	− 14.4	0.277
SL58-3	Biotite granite porphyry	− 12.3	0.464
SL58-4	Biotite granite porphyry	− 14.0	0.253
SL58-5	Biotite granite porphyry	− 13.6	0.235
SL58-6	Biotite granite porphyry	− 13.8	0.244
SL58-7	Biotite granite porphyry	− 13.8	0.254
SL25-1	Sandstone	− 14.9	0.297
SL25-2	Sandstone	− 15.2	0.306
SL25-3	Sandstone	− 14.7	0.322
SL25-4	Sandstone	− 14.6	0.328
SL25-5	Sandstone	− 15.0	0.317
SL25-6	Sandstone	− 13.8	0.463
SL25-7	Sandstone	− 15.1	0.344
SL25-8	Sandstone	− 14.0	0.336
SL25-9	Sandstone	− 13.5	0.33
SL25-10	Sandstone	− 14.2	0.347
SL25-11	Sandstone	− 13.3	0.34

to the formation of tourmaline were predominantly derived from the rhyolitic melt.

6.2 Compositional variations in tourmaline

Tourmaline in the Longtoushan deposit belongs mainly to the schorl-dravite series, and can be divided into five types with respect to host rock. One cluster of tourmaline analyses from the rhyolite porphyry fell in field 2 in the Fe_{tot}–Mg–Al triangular diagram, suggesting a formation environment similar to Li-poor granitoids. Moreover, some tourmalines in this cluster had high Fe/(Fe + Mg) and X vacancy/(Na + X vacancy), while others had relatively low Fe/(Fe + Mg) and X vacancy/(Na + X vacancy) (see Fig. 7). Based on petrographic features, a large number of potassium feldspar crystals have been replaced by tourmaline in the rhyolite porphyry rock. Hence, like tourmaline nodules described by Yang et al. (2015), the tourmalines with high Fe/(Fe + Mg) ratios from the rhyolite porphyry exhibited magmatic-hydrothermal features related to the exsolution, phase separation, and entrapment of immiscible aqueous boron-rich fluids. However, the tourmalines with low Fe/(Fe + Mg) ratios and tourmaline from the cryptoexplosive breccia, monzogranite porphyry, biotite granite porphyry, and sandstone fell dominantly within fields 4 and 5 (Fig. 6b). This may be the result of post-magmatic hydrothermal alteration caused by the infiltration of boron-rich fluids. Additionally, a small group of tourmalines from sandstone fell within field 6, suggesting the presence of Fe^{3+} (Henry and Guidotti 1985). The presence of Fe^{3+} indicates that those tourmalines crystallized in a relatively oxidized fluid system.

A wide variation in the Fe/(Fe + Mg) ratio reflects the exchange vector $MgFe_{-1}$ in tourmaline with different occurrences, whereas values of $\sum(Fe + Mg) < 3$ apfu (atoms per formula unit) reveal the negligible presence of Fe^{3+} (Fig. 8a–d). Substantial amounts of Al were incorporated in the Y-site via the $Al\square(NaR^{2+})_{-1}$ substitutions in tourmaline, where R = Fe, Mg (Fig. 8e–h). The X-site vacancies versus Al diagram (Fig. 8e–h) permits separating the influence of the $AlO(R^{2+}OH)_{-1}$ and $FeAl_{-1}$ exchanges from the $Al\square(NaR^{2+})_{-1}$ exchange for the different types of tourmaline. The influence of the $FeAl_{-1}$ exchange mechanism was negligible in tourmaline from the rhyolite porphyry, cryptoexplosive breccia, biotite granite porphyry, and monzogranite porphyry, although relatively large in tourmaline from the sandstone. With respect to the correlation between Na and Ca at the X-site (Fig. 8i–l), tourmaline from the deposit was predominately controlled by $(\square Al)\ (NaMg)_{-1}$. In addition, as shown in Fig. 8i–l, there was locally a vector corresponding to $(CaMg)\ (NaAl)_{-1}$ in tourmaline from the cryptoexplosive breccias and sandstone, which may be controlled by the host rock.

Tourmaline that crystallized in the post-magmatic-hydrothermal stage generally shows dravitic compositions and exhibits some compositional zoning in BSE images (e.g. Fig. 2c). The Longtoushan gold deposit is controlled by breccia pipe and faults (Huang et al. 1999), suggesting a fluid-dominated system, which indicates that tourmaline chemistry is generally buffered by the fluid phase. Electron microprobe analyses revealed that there are considerable variations in Ti, Fe, Mg, and Na contents in the oscillatory zones, and negligible variations of other elements (see Fig. 9). Darker-colored zones exhibit relatively higher Mg

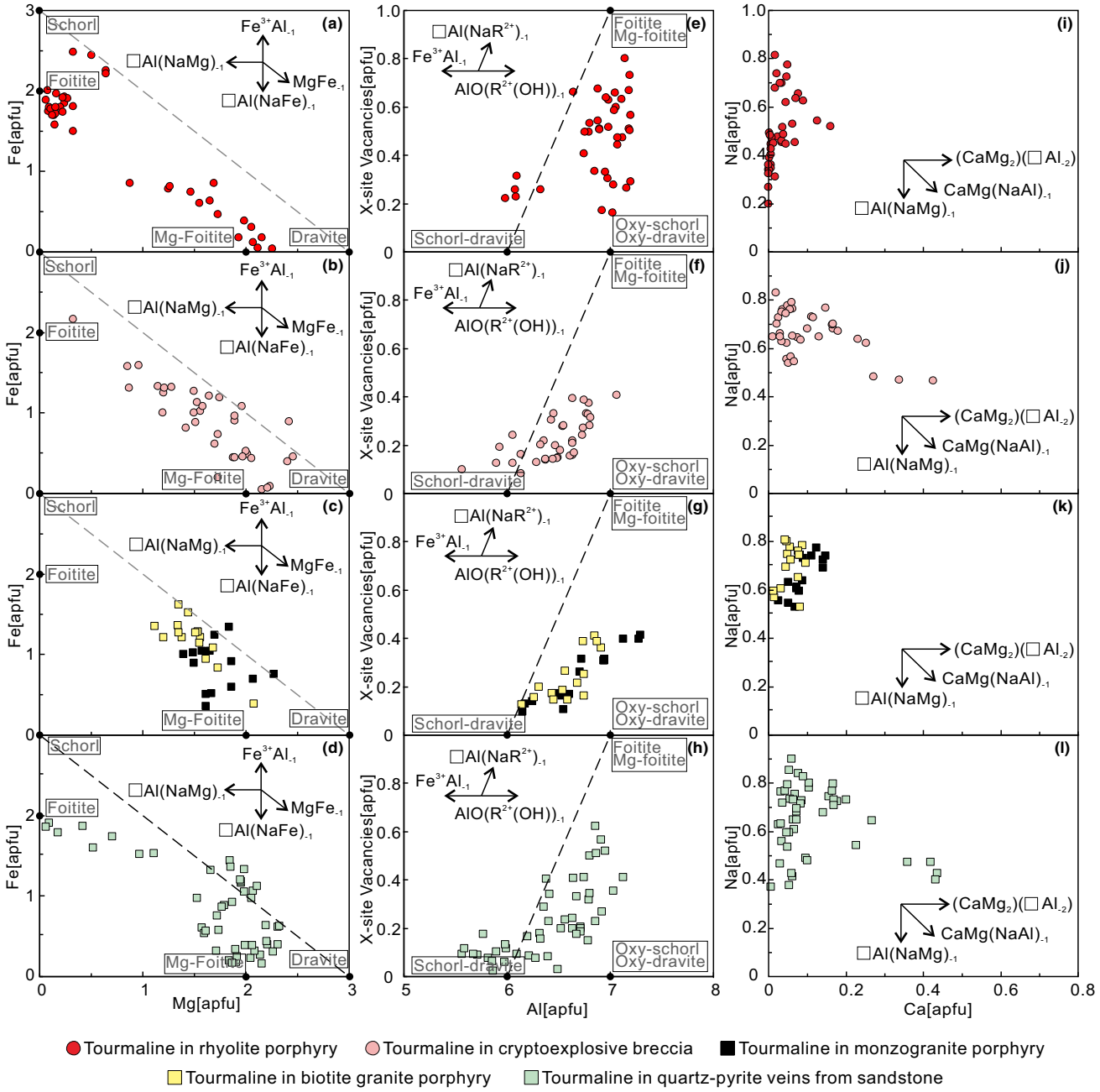

Fig. 8 Chemical compositions of tourmaline from the Longtoushan deposit expressed in terms of atomic ratios and atoms per formula unit (apfu). **a–d** Mg (apfu) versus Fe (apfu); **e–h** Al (apfu) versus X-site vacancies (apfu); **i–l** Ca (apfu) versus Na (apfu)

content and lower Ti and Fe content, whereas lighter-colored zones exhibit the opposite. In Fig. 9, the increase in Na content from core to rim in tourmaline is consistent with experimental results (Goerne et al. 2001) indicating that Na content increases with decreasing temperature. Moreover, the higher Fe content in the rims suggests a temperature decrease (Mlynarczyk and Williams-Jones 2006).

6.3 Implications for gold mineralization

Alkaline solutions produce boron complexes that are typically tetrahedrally coordinated with oxygen in $[B(OH)_4]^-$ anionic complexes. Nevertheless, boron is triangularly coordinated with three oxygens in a $B(OH)_3$ complex in neutral to acidic conditions, which is consistent with the coordination of boron in tourmaline (Meyer et al. 2008; Dutrow and Henry 2011). The amount of boron required to stabilize tourmaline increases with increasing pH, and

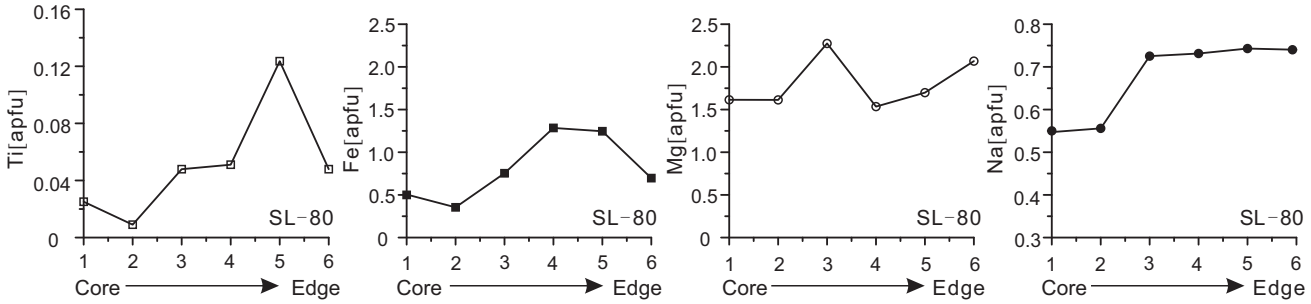

Fig. 9 Line plot of the content of Ti, Fe, Mg, and Na in tourmaline zonation from monzogranite porphyry

tourmaline has not yet been synthesized under alkaline conditions (Morgan and London 1989). Thus, tourmaline is stable in highly acidic to neutral solutions (Morgan and London 1989; Henry and Dutrow 1996). In the Longtoushan deposit, a large number of potassium feldspar crystals have been replaced by tourmaline in the cryptoexplosive breccia and rhyolite porphyry. The reaction can be described as follow.

$$\begin{aligned} &3B(OH)_3 + Na^+ + 6K(AlSi_3O_8)(\text{Potassium feldspar}) \\ &\quad + 3\left(Mg^{2+}, Fe^{2+}\right) \\ &= Na(Mg, Fe)_3Al_6Si_6O_{18}(BO_3)_3(OH)_4(\text{Tourmaline}) \\ &\quad + 12SiO_2(\text{Quartz}) + 6K^+ + H^+ + 2H_2O \end{aligned}$$

Gold is deposited both with tourmaline and partly after tourmalinization (Xie and Sun 1993; Huang et al. 1999). The tourmaline precipitated from fluids with temperature ranging from 320 to 560 °C, and the anions in the fluids were dominated by Cl^- (Huang et al. 1999). According to Williams-Jones et al. (2009), $AuCl_2^-$ is likely to be the main control on the solubility of gold in chloride-rich systems at temperatures above 350 °C, and cooling is effective in causing large-scale deposition of gold transported as chloride complexes. Therefore, $AuCl_2^-$ was the dominant form of gold in hydrothermal solutions during the early stages of mineralization in the Longtoushan deposit, and cooling was effective in causing low-grade gold mineralization in the rhyolite porphyry and its wall rock. However, in tourmalines from the rhyolite porphyry, cryptoexplosive breccia, monzogranite porphyry, and biotite granite porphyry, negligible substitution of Fe^{3+} for Al indicates that the tourmalines were deposited from a relatively reduced fluid system (Trumbull et al. 2011). H^+ was released during the replacement of potassium feldspar by tourmaline, leading to a decrease in pH of the fluids. Furthermore, $[Au(HS)_2]^-$ and Au(HS) are the dominant forms of gold in hydrothermal solutions at mineralization temperatures below 350 °C (Williams-Jones et al. 2009). Consequently, the solubility of gold may have increased due to the increased stability of bisulfide species after an initial decrease in the Longtoushan deposit. In addition, abundant coexisting liquid-rich and vapor-rich inclusions are indicative of boiling, and the occurrence of native gold is closely related to pyrite in the Longtoushan deposit (Huang et al. 1999). The gold would be transported to the fractures and faults, and deposited by other controlling factors, such as boiling and sulfidation, which is consistent with the occurrences of native gold and gold orebodies in the Longtoushan deposit (Xie and Sun 1993).

7 Conclusions

(1) Tourmaline is enriched in the contact zone between rhyolite porphyry and cryptoexplosive breccia in the Longtoushan deposit. The NW-striking trend of the tourmaline enrichment zones is similar to that of the gold orebody.

(2) Tourmalines dominantly plot within the field of the schorl-dravite series. The tourmalines belong mainly to the alkali group and partly to the X-vacant group. The bimodality in chemical compositions of tourmaline from the rhyolite porphyry reflects that one group formed in the magmatic-hydrothermal stage and the other in the post-magmatic hydrothermal stage. However, most tourmalines from the Longtoushan deposit crystallized during the post-magmatic hydrothermal stage.

(3) Calculated $\delta^{11}B$ values for the mineralizing fluids ranged from − 12.8 to − 9.7‰, which is typical of S-type granites, and the boron-enriched fluids predominantly derived from the rhyolitic melt.

(4) The tourmalines were deposited from a relatively reduced and acidic fluid system, and the gold in the Longtoushan deposit was predominantly precipitated in the post-magmatic hydrothermal stage.

Acknowledgements This study was supported by the Project of Innovation-driven Plan in Central South University (Project No. 2015CX008) and the Fundamental Research Funds for the Central Universities of Central South University (Project No. 2015zzts071). Miao Yu and Jeff Dick are thanked for their critical review of the

manuscript. Moreover, we wish to thank two anonymous reviewers and editors for their constructive comments.

References

Bureau of Geology and Mineral Resources of Guangxi Zhuang Autonomous Region (1985) Regional geology of Guangxi Zhuang Autonomous Region. Geological Publishing House, Beijing **(in Chinese)**

Chen MH, Li ZY, Li Q et al (2015) A preliminary study of multi-stage granitoids and related metallogenic series in Dayaoshan area of Guangxi, China. Earth Sci Front 22:41–53. https://doi.org/10.13745/j.esf.2015.02.004 **(in Chinese with English abstract)**

Chen FW, Li HQ, Mei YP (2008) Zircon SHRIMP U-Pb chronology of diagenetic mineralization of the Longtoushan porphyry gold orefield, Gui County, Guangxi. Acta Geol Sin (Chin Ed) 82:921–926 **(in Chinese with English abstract)**

Codeço MS, Weis P, Trumbull RB et al (2017) Chemical and boron isotopic composition of hydrothermal tourmaline from the Panasqueira W–Sn–Cu deposit, Portugal. Chem Geol 468:1–16. https://doi.org/10.1016/j.chemgeo.2017.07.011

Duan RC, Ling WL, Li Q et al (2011) Correlations of the late Yanshanian Tectonomagmatic events with metallogenesis in South China: geochemical constraints from the Longtoushan gold ore deposit of the Dayaoshan area, Guangxi Province. Acta Geol Sin (Chin Ed) 85:1644–1658 **(in Chinese with English abstract)**

Dutrow BL, Henry DJ (2011) Tourmaline: a geologic DVD. Elements 7:301–306. https://doi.org/10.2113/gselements.7.5.301

Goerne GV, Franz G, Heinrich W (2001) Synthesis of tourmaline solid solutions in the system Na_2O–MgO–Al_2O_3–SiO_2–B_2O_3–H_2O–HCl and the distribution of Na between tourmaline and fluid at 300 to 700 °C and 200 MPa. Contrib Mineral Petrol 141:160–173. https://doi.org/10.1007/s004100100243

Henry DJ, Dutrow BL (1996) Metamorphic tourmaline and its petrologic applications. In: Grew ES, Anovitz LN (eds) Boron: mineralogy, petrology, and geochemistry, vol 33. Mineralogical Society of America, Chantilly, pp 503–557

Henry DJ, Guidotti CV (1985) Tourmaline as a petrogenetic indicator mineral: an example from the staurolite-grade metapelites of NW Maine. Am Mineral 70:1–15

Henry DJ, Novák M, Hawthorne FC et al (2011) Nomenclature of the tourmaline-supergroup minerals. Am Mineral 96:895–913. https://doi.org/10.2138/am.2011.3636

Hervig RL, Moore GM, Williams LB et al (2002) Isotopic and elemental partitioning of boron between hydrous fluid and silicate melt. Am Mineral 87:769–774

Hinsberg VJV, Henry DJ, Marschall HR (2011) Tourmaline: an ideal indicator of its host environment. Can Mineral 49:1–16. https://doi.org/10.3749/canmin.49.1.1

Hou KJ, Li YH, Xiao YK, Tian YR (2010) In situ boron isotope measurements of natural geological materials by LA-MC-ICP-MS. Chin Sci Bull 55:3305–3311 **(in Chinese with English abstract)**

Huang MZ, Chen WS, Li WZ et al (1999) Longtoushan gold deposit of subvolcanic-cryptoexplosion breccia type, Guangxi. Acta Geosci Sin 20:39–46 **(in Chinese with English abstract)**

Huang HM, He ZJ, Cui B (2003) Metallogenic series of granite in Dayaoshan of Guangxi. Geol Prospect 39:12–16 **(in Chinese with English abstract)**

Huang XY, Zhang H, Tang Y, Guan SJ (2008) Chemical composition of tourmalines from the B-rich granite and miarolitic cavities in Yinping, Guangxi and its implications for evolution of the magmatic-hydrothermal system. Acta Mineral Sin 28:25–34. https://doi.org/10.16461/j.cnki.1000-4734.2008.01.003 **(in Chinese with English abstract)**

Jiang SY, Palmer MR, Slack JF, Shaw DR (1999) Boron isotope systematics of tourmaline formation in the Sullivan Pb–Zn–Ag deposit, British Columbia, Canada. Chem Geol 158:131–144. https://doi.org/10.1016/S0009-2541(99)00023-6

Lu ZL (2008) Chinese tourmaline deposits' types with their geological characteristics. Miner Resour Geol 22:174–178 **(in Chinese with English abstract)**

Mao JW, Chen MH, Yuan SD, Guo CL (2011) Geological characteristics of the Qinhang (or Shihang) metallogenic belt in South China and spatial-temporal distribution regularity of mineral deposits. Acta Geol Sin 85:636–658 **(in Chinese with English abstract)**

Marschall HR, Korsakov AV, Luvizotto GL et al (2009) On the occurrence and boron isotopic composition of tourmaline in (ultra) high-pressure metamorphic rocks. J Geol Soc Lond 166:811–823. https://doi.org/10.1144/0016-76492008-042

Meyer C, Wunder B, Meixner A et al (2008) Boron-isotope fractionation between tourmaline and fluid: an experimental re-investigation. Contrib Mineral Petrol 156:259–267. https://doi.org/10.1007/s00410-008-0285-1

Mlynarczyk MSJ, Williams-Jones AE (2006) Zoned tourmaline associated with cassiterite: implications for fluid evolution and tin mineralization in the San Rafael Sn–Cu deposit, southeastern Peru. Can Mineral 44:347–365. https://doi.org/10.2113/gscanmin.44.2.347

Morgan GB, London D (1989) Experimental reactions of amphibolite with boron-bearing aqueous fluids at 200 MPa: implications for tourmaline stability and partial melting in mafic rocks. Contrib Mineral Petrol 102:281–297

Novák M, Skoda R, Filip J et al (2011) Compositional trends in tourmaline from intragranitic NYF pegmatites of the trebic pluton, Czech Republic: an electron microprobe, Mossbauer and LA-ICP-MS study. Can Mineral 49:359–380. https://doi.org/10.3749/canmin.49.1.359

Palmer MR, Slack JF (1989) Boron isotopic composition of tourmaline from massive sulphide deposit and tourmalinites. Contrib Mineral Petrol 103:434–451

Slack JF (1996) Tourmaline associations with hydrothermal ore deposites. Rev Mineral Geochem 33:559–643

Slack JF, Coad PR (1989) Multiple hydrothermal and metamorphic events in the Kidd Creek volcanogenic massive sulphide deposit, Timmins, Ontario: evidence from tourmalines and chlorites. Can J Earth Sci 26:694–715. https://doi.org/10.1139/e89-059

Slack JF, Trumbull RB (2011) Tourmaline as a recorder of ore-forming processes. Elements 7:321–326. https://doi.org/10.2113/gselements.7.5.321

Tao SL, Lai JQ, Zhang JD et al (2017) Geochemical characteristics of auriferous pyrite in Longtoushan gold deposit, Guangxi Province, China. Chin J Nonferrous Met 27:1263–1279. https://doi.org/10.19476/j.ysxb.1004.0609.2017.06.022 **(in Chinese with English abstract)**

Tonarini S, Pennisi M, Adorni-Braccesi A et al (2003) Intercomparison of boron isotope and concentration measurements. Part I: section, preparation and homogeneity tests of the intercomparison materials. Geostand Geoanal Res 27:21–29. https://doi.org/10.1111/j.1751-908X.2003.tb00710.x

Trumbull RB, Slack JF, Krienitz M-S et al (2011) Fluid sources and metallogenesis in the Blackbird Co–Cu–Au–Bi–Y–REE district, Idaho, U.S.A.: insights from major-element and boron isotopic compositions of tourmaline. Can Mineral 49:225–244. https://doi.org/10.3749/canmin.49.1.225

Trumbull RB, Slack JF (2018) Boron isotopes in the continental crust: granites, pegmatites, felsic volcanic rocks, and related ore

deposits. In: Marschall HR, Foster GL (eds) Boron isotopes: the fifth element (advances in isotope geochemistry). Springer, Berlin

Wang CH (2011) Metallogenic model and prognosis of the Longtoushan gold field, the Guangxi Zhuang Autonomous Region, China. Dissertation, Chinese Academy of Geological Sciences **(in Chinese)**

Williams-Jones AE, Bowell RJ, Migdisov AA (2009) Gold in solution. Elements 5:281–287. https://doi.org/10.2113/gselements.5.5.281

Xie LS, Sun BD (1993) Geological characteristics of Longtoushan volcanic–subvolcanic gold deposit, Guigang City, Guangxi. Geol Guangxi 6:27–42 **(in Chinese with English abstract)**

Xiong X, Xu WY, Lv QT et al (2014) Tourmaline as an early stage indicator of uranium mineralization in the deep drilling, Luzong Basin, Anhui Province. Acta Petrol Mineral 33:263–272 **(in Chinese with English abstract)**

Yang SY, Jiang SY, Palmer MR (2015) Chemical and boron isotopic compositions of tourmaline from the nyalam leucogranites, south Tibetan Himalaya: implication for their formation from B-rich melt to hydrothermal fluids. Chem Geol 419:102–113

Yang GG, Zhu WF, Zhang F (2008) Multistage ore-forming process and distributing characteristics of Au, Ag elements in the Longtoushan gold deposit, Guangxi. Miner Resour Geol 22:437–440 **(in Chinese with English abstract)**

Zhou YZ, Zeng CY, Li HZ et al (2012) Geological evolution and ore-prospecting targets in southern segment of Qinzhou Bay–Hangzhou Bay juncture orogenic belt, southern China. Geol Bull China 31:486–491 **(in Chinese with English abstract)**

Zhu GT (2002) Study on geological character and genesis of Longtoushan gold deposit of Guangxi. Miner Resour Geol 16:266–272 **(in Chinese with English abstract)**